Title

How thermal fluctuations influence the function of the FeMo cofactor in nitrogenase enzymes

Journal

Chem Catalysis, 3(7)

ISSN

2667-1107

Authors

Li, Wan-Lu
Li, Yong
Li, Jun
et al.

Publication Date

2023-07-01

DOI

10.1016/j.checat.2023.100662

How Thermal Fluctuations Influence the Function of the FeMo-cofactor in Nitrogenase Enzymes

Wan-Lu Li[1,3], Yong Li[4,5,7], Jun Li[4,6], Teresa Head-Gordon[1–3]

[1]Kenneth S. Pitzer Theory Center and Department of Chemistry,
[2]Departments of Bioengineering and Chemical and Biomolecular Engineering
University of California, Berkeley, CA, 94720 USA
[3]Chemical Sciences Division, Lawrence Berkeley National Laboratory, Berkeley, CA, 94720 USA
[4]Department of Chemistry and Engineering Research Center of Advanced Rare-Earth Materials of Ministry of Education, Tsinghua University, Beijing, 100084, China
[5]Institute of Applied and Physical Chemistry and Center for Environmental Research and Sustainable Technology, University of Bremen, Bremen, 28359, Germany
[6]Department of Chemistry and Guangdong Provincial Key Laboratory of Catalytic Chemistry, Southern University of Science and Technology, Shenzhen 518055, China
[7]Department of Chemistry-Ångström Laboratory, Uppsala University, Uppsala, 75121, Sweden
Corresponding authors: yongli.uni@gmail.com; junli@tsinghua.edu.cn; thg@berkeley.edu
Lead contact email address: thg@berkeley.edu

Abstract

The catalytic mechanism of N_2 fixation by nitrogenase remains unresolved in how the strong N≡N bond is activated and why the reductive elimination of H_2 is required. Here we use Density Functional Theory and physiologically relevant thermal simulations to elucidate the mechanism of the complete nitrogenase catalytic cycle. Over the accumulation of four reducing equivalents we find that protons and electrons transfer to the FeMo-cofactor to weaken and break its bridge Fe-S bond, leading to temporary H_2S formation that exposes the Fe sites to weakly bind N_2. Remarkably, we find that subsequent H_2 formation is responsible for chemical activation to an N=N double bond accompanied by a low barrier for H_2 release. We emphasize that finite temperature effects smooth out mechanistic differences between DFT functionals observed at 0 K, thus leading to a consistent understanding as to why H_2 formation is an obligatory step in N_2 adsorption and activation.

INTRODUCTION

The nitrogenase enzyme can absorb and activate the strong N≡N triple bond at ambient conditions to catalyze the reduction reaction of N_2 to NH_3, thereby providing a biological fixation route to more than half of the nitrogen needed to sustain the human population on earth[1–5]. The total dinitrogen hydrogenation process, $N_2 + 3\ H_2 \rightarrow 2NH_3$, is net exothermic, and more so if activated hydrogen in the form of solvated H^+/e^- is utilized. However, the first bond cleavage of the N_2 molecule requires enthalpy $\Delta H \approx 4.7$ eV at standard temperature and pressure, which is almost one-half the value for full N_2 dissociation (9.7 eV)[6]. Furthermore, the large HOMO-LUMO gap (ca. 10 eV)[6] and the low proton binding energy (5.1 eV) of N_2 make the processes of electron and proton transfer to N_2 very difficult at the beginning of the nitrogen fixation reaction. Therefore, there is great interest in the molecular-level understanding of how the nitrogenase enzyme achieves this challenging task. Significantly, elucidating the biological mechanism of nitrogen fixation would also be useful and insightful in the development of more efficient catalysts for industrial ammonia synthesis.

Nitrogenases are widely distributed in nature, and the corresponding genes required for production are found in 13 bacterial phyla and one archaeal phylum. MoFe, VFe, FeFe proteins are three known isozymes of nitrogenase[9–12] of which MoFe protein is the predominant and the most active isozyme[13] and VFe and FeFe are often called "alternative" nitrogenases as many diazotrophs carry genes for at least one[14]. The quaternary structures of VFe and FeFe nitrogenases have been reviewed elsewhere[5,15,16]. Our work mainly focuses on the FeMo cofactor (FeMo-co) in the hetero-tetrameric MoFe protein (Figure 1a) which is the functional catalytic unit with a triangular prism Fe_7MoCS_9 cluster that utilizes supplied electrons and protons (from $(H_2O)_nH^+$ chains[17]) to reduce the N_2. The stoichiometry of the nitrogenase-catalyzed nitrogen fixation under ambient conditions is experimentally identified by the reaction in Eq. (1)

$$N_2 + 8H^+ + 8e^- + 16ATP \rightarrow 2NH_3 + H_2 + 16ADP + 16Pi \tag{1}$$

where ATP, ADP, and Pi are the metabolites adenosine triphosphate, adenosine diphosphate, and an

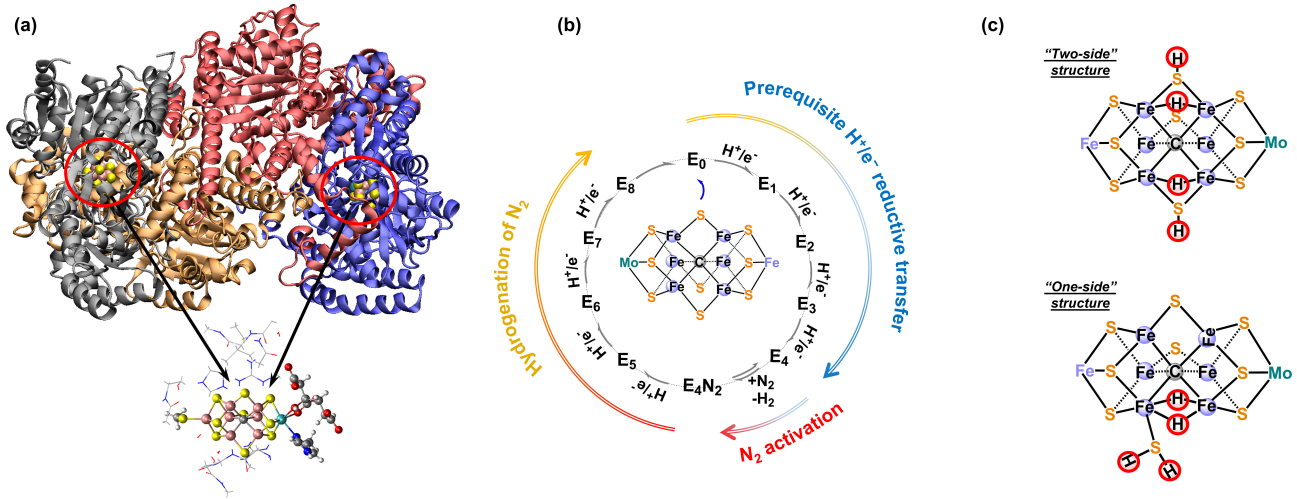

Figure 1: *The nitrogenase enzyme and FeMo-co unit used to execute the catalytic steps for nitrogen fixation over a complete cycle.* (a) the MoFe protein (PDB ID: 3U7Q)[7] with FeMo-co center highlighted in the ball and stick model below. (b) The whole catalytic cycle of nitrogen fixation by nitrogenase from steps $\mathbf{E}_1$ to $\mathbf{E}_8$ based on the Lowe-Thorneley kinetic model[8]. Further details are provided in supplemental information. (c) The FeMo-co structures of the two-side (2S) and one-side (1S) configurations for the $\mathbf{E}_4$ state. The adsorbed H atoms are circled in red.

inorganic orthophosphate, respectively.[8] Utilizing the energy released from the hydrolysis of coenzyme ATP, the electrons are transferred from the Fe protein to the MoFe protein, where NH_3 and obligatory H_2 are generated on the FeMo-co subunit[1,18,19]. The Lowe-Thorneley (LT) model[8] describes the transformations and kinetics among catalytic intermediates (denoted $\mathbf{E}_n$) for which eight H^+/e^- reducing equivalents delivered to the FeMo-co center ultimately create the NH_3 reductive product (Figure 1b). The LT model assumes that ten main intermediates are involved in the entirety of nitrogen bio-fixation reactions, although the detailed reaction mechanism might contain even more intermediates for H^+/e^- pair transfers, N_2 activation, H_2 formation, N_2 protonation, and NH_3 production.

Despite the numerous experimental efforts that have been carried out to explore nitrogenase and its catalytic mechanism, the crystallographic structures of the $\mathbf{E}_1$ to $\mathbf{E}_8$ intermediate states are difficult to detect due to their labile nature. Crystal structures of putative bound -N_2- species have been reported by Ribbe and Hu[20] but have been questioned[21,22] due to the absence of external reductants that may not fully distinguish the reported state from the oxidized MoFe protein. Thus, many mechanistic aspects of the nitrogenase-catalyzed N_2 fixation reaction remains unknown[1,2,19]. Theoretical investigations to explore and identify the possible activated species and intermediates in the nitrogenase cycle have become essential to fully understand the mechanism[2]. Neese and Bjornsson have thoroughly uncovered the electronic structure of FeMo-co using quantum chemical calculations along with experimental measurements, including the oxidation states of Mo and Fe centers, net charges, and its magnetic properties have been widely reported[3,23–25]. The prerequisite protonations of FeMo-co and the hydrogenation of N_2 have been reported in the theoretical literature based on chemical models that typically rely on Density Functional Theory (DFT).[26] Using the BP86 GGA functional[27], Hoffman and co-workers proposed an $\mathbf{E}_4$ state with a "two-side" (2S) structure (Figure 1c), where the adsorption sites of hydrogen atoms occur on two sides of the bridged sulfurs[28–30], to create a weakly bound N_2[28] Using a hybrid functional, Siegbahn has suggested a four-electron preactivation of the FeMo cluster, before the catalytic $\mathbf{E}_0$ state is formed[31,32] (see also the supplemental information), but Hoffman et al. have argued that such a proposed structure is inconsistent with experimental measurements[29]. Ryde's group carried out systematic calculations with different exchange-correlation functionals, particularly for the N_2 hydrogenation steps by considering the pathways with or without dissociation of the sulfur bridge[33–36]. Very recently, they validated the resting state ($Fe_3^{II}Fe_4^{III}Mo^{III}$) of $\mathbf{E}_0$ with the calculation of redox potentials by quantum mechanical methods[37]. However, the reason why H_2 formation is crucial and obligatory and the detailed N_2 activation steps, in particular the creation of the activated N=N double bond[30,33,38], are still open research questions. Additional clues in the nitrogenase story include inhibitor studies of MoFe-protein using carbon monoxide[39,40], hydroxo[41] and selenium[42], and provide powerful tools to prepare the stably trapped transient states and indicate the activation of N_2 occurs on a di-iron edge of FeMo-co. A recent study reported that the dissociated HS^- species can be held within a protein cavity created by the reorientation of glutamine in V-nitrogenase[43]. Together with the facile exchange of all the three bridged sulfur sets, and the lability of the S2B towards ligand exchange found from experiments of site-selective incorporation of selenium in FeMo-co[42,44], this sets up the possibility of partial or full dissociation of bridged S2B from FeMo-co as recently discussed by us and other theoretical work[45–50].

In addition to choice of exchange-correlation functional, the greater environment of the protein is required beyond an isolated FeMo-co catalytic center. A number of state-of-the-art QM/MM studies, especially on the $\mathbf{E}_2$ and $\mathbf{E}_4$ states, have been performed by the groups of Ryde and Bjornsson that well describe the long-range chemical interactions emanating from the protein scaffold and due to solvent[30,47,51,52]. Raugei et al.[53] have developed an extended cluster model of FeMo-co within a corona of amino acids, showing that it is a necessary ingredient when considering the energetics of the $\mathbf{E}_4$ state in particular. Moreover, nitrogenase operates its catalytic function under ambient temperature, and therefore thermal motions might influence the energetic stability of various intermediates that is crucial to understand and reveal the catalytic mechanism of the total reaction profile[54,55]. We wish to especially acknowledge the fact

that all enzymes exhibit low activity at cold temperatures and are only fully active at an optimal finite temperature. For example, thermally averaged motions found from room-temperature X-ray crystallography have been shown to be important for enzyme catalysis[53], and statistical fluctuations of active site residues are productively utilized for enzyme turnover events for Ketosteroid isomerase[56], add further nuance to pre-organized electric fields[57,58] as well as effecting the catalytic barrier[59]. However, to the best of our knowledge, no study has examined the effect of thermal fluctuations on the entire FeMo-co catalytic mechanism for nitrogenase.

Based on an extended cluster model of FeMo-co that includes directly contacting protein residues[53], with an implicit solvent environment beyond that, we consider the energetics of the LT kinetic model of the complete cycle[8] using *ab initio* molecular dynamic (AIMD) and metadynamic simulations, with two different DFT functionals to ensure that conclusions are consistent across quantum mechanical models. Only when we consider a statistical thermodynamic perspective do we find that both functionals (Meta-GGA-B97M-rV and GGA-BP86) independently and consistently predict a "one-side" (1S) mechanism (Figure 1c), i.e. H adsorption occurs on the same side of bridged sulfur (S2B) with further subsequent H_2S formation, which is conducive to exposing two Fe coordination sites to subsequently adsorb N_2. Remarkably, the accounting of thermal motion lowers the barrier to H_2 release that then activates the N_2 triple bond to undergo a chemical change to a double bond, thereby explaining why H_2 is an obligatory step in the nitrogenase enzyme mechanism.

RESULTS AND DISCUSSION

There are three possible states proposed by experimental studies for the $\mathbf{E}_0$ state: the resting or native state (FeMo-co^N), the one-electron reduced state (FeMo-co^{Red}), and the one-electron oxidized state (FeMo-co^{Ox})[1]. It is of primary importance to determine the relations between these three experimentally identified states for $\mathbf{E}_0$ in regards initializing the reaction. Based on extensive experimental analysis of the oxidation and spin state found by methods such as Mössbauer and ENDOR spectroscopy[60–62], and described thoroughly as depicted in Figure S2, the $\mathbf{E}_0$ state is proposed to have an electronic configuration of $Fe_3^{II}Fe_4^{III}Mo^{III}$ with S = 3/2. The protonation state of the homocitrate ligand is also expected to have a strong impact on the reactivity of the active center. In accordance with the QM/MM results performed by Cao et al.[63], we herein apply the triply deprotonated form (net charge -3) for homocitrate as shown in Figure S3, with a proton shared between the alcohol group coordinated to Mo and one of the carboxylate groups that is consistent with crystallographic refinement[64].

According to the FeMo-co cluster model by Raugei et al.[53] shown in Figure S1 and Figure 2a, the BP86 functional yields the lowest mean absolute deviations (MADs) for the geometric parameters of the $\mathbf{E}_0$ state (Figure 2b) at both 0 K and 300 K compared with experiment[7], supporting its popularity for describing metallo-enzymatic systems[28]. The semiempirical meta-GGA functional B97M-rV[65,66] has also shown promise by correctly describing the intermolecular interactions of many molecular systems[67–69] and has accurately predicted surface relaxations and CO adsorption energies for precious metal electrocatalysts consistent with experimental findings in the NVT ensemble[54]. Therefore, we also considered the B97M-rV performance on the same metalloenzymatic system for the full LT catalytic cycle. We find that the calculated bond lengths in the FeMo-co center for $\mathbf{E}_0$ using B97M-rV are overestimated but with a MAD that is acceptable upon inclusion of thermal effects (0.075 Å). By comparing the geometric parameters of the $\mathbf{E}_0$ state obtained at 0 K and 300 K, as listed in Table S1, it can be concluded that the thermal effect has a minor impact on the geometries of the $\mathbf{E}_0$ state.

Prerequisite H^+/e^- reductive transfers before N_2 activation

The first four protonation processes of H^+/e^- pair-transfers to the FeMo-co center have been suggested to be the preparation for N_2 binding[1,70,71]. Although the possible protonated structures for $\mathbf{E}_1$ through $\mathbf{E}_4$ have been reported previously[28,72,73], it is still debatable as to which is the most energetically stable structure at each $\mathbf{E}_n$ step. In addition, the [Fe-H-Fe] metal-hydride bonds in some organometallic catalysts have been reported to play a key role in the adsorption and activation of the N_2 molecule[6], and also found to be relevant for the FeMo-co structure by ^{1,2}H and ^{95}Mo ENDOR experiments[74,75]. But because FeMo-co is a quasi-symmetric triangular prism with three facets for reactions, what is the hydride structure formed during the early H^+/e^- transfer stages is not fully known, although experimental mutation studies have implicated that hydride adsorption occurs on a single facet, "f1", defined by Fe2-S2B-Fe6-S5A[76–78].

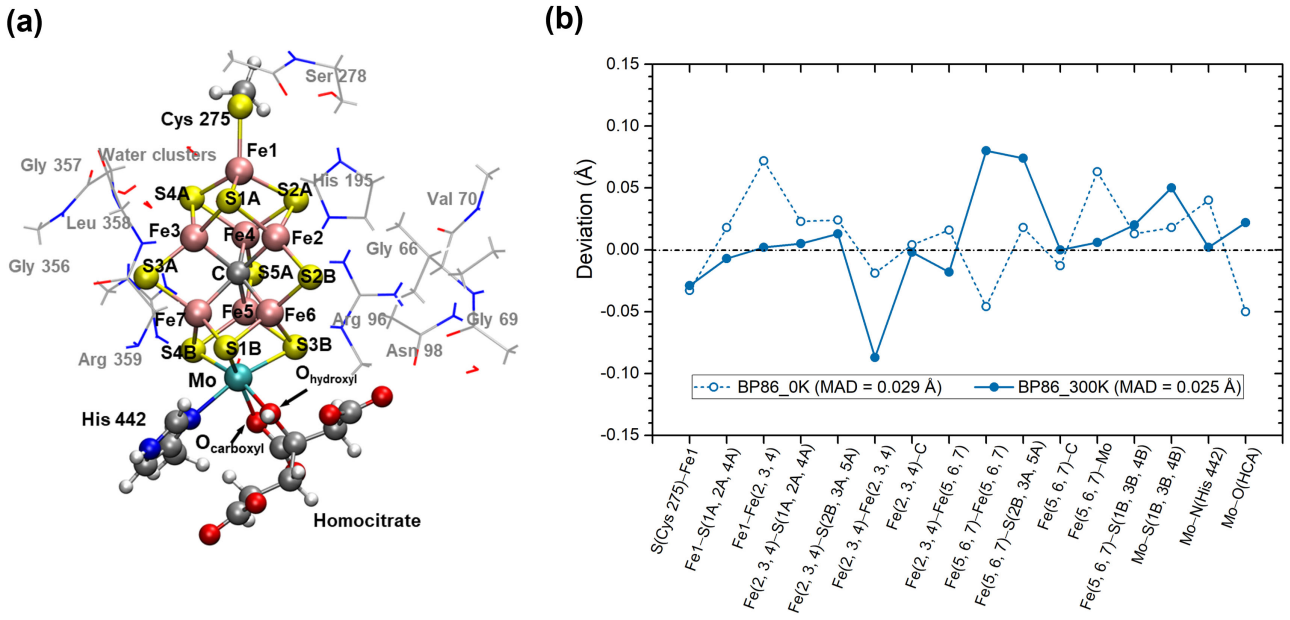

Figure 2: *The FeMo-co computational model and agreement between the bonded structure of the* $\boldsymbol{E}_0$ *state from BP86 and experiment.* (a) The cluster model, with an extended protein environment of FeMo-co due to Raugei and co-workers[28] in the context of the surrounding key residues (labels in grey), where all the residues and water molecules engaging hydrogen-bonding interaction with FeMo-co are included in the model, as well as a more complete model of homocitrate[63]. Color code: H-white, C-gray, N-blue, O-red, S-yellow, Fe-lilac, Mo-cyan. (b) Bond-length deviations calculated at the level of BP86, with and without thermal statistics, compared to the PDB structure (PDB ID: 3U7Q)[7]. The Mean Absolute Deviations (MAD) values are shown in parentheses. Similar calculations using the B97M-rV functional are provided in Table S1.

The structure of the key $\mathbf{E}_4$ state[19,38,79,80] has been called the "Janus intermediate" since it has been experimentally suggested to contain two [Fe-H-Fe] bridging hydrides and can react in both directions for releasing H_2 or desorbing N_2[1,5,75]. Yet, it has not been possible to deduce an unambiguous picture of the spatial relationships of the two hydride bridges by experiment[1,5], and therefore theoretical studies have become essential to fill in this structural picture. The decision of whether the H adsorption occurs on a 1S *vs* 2S structure of the bridged sulfurs (Figure 1c) can lead to a dramatically different conclusion regarding N_2 activation and H_2 release.

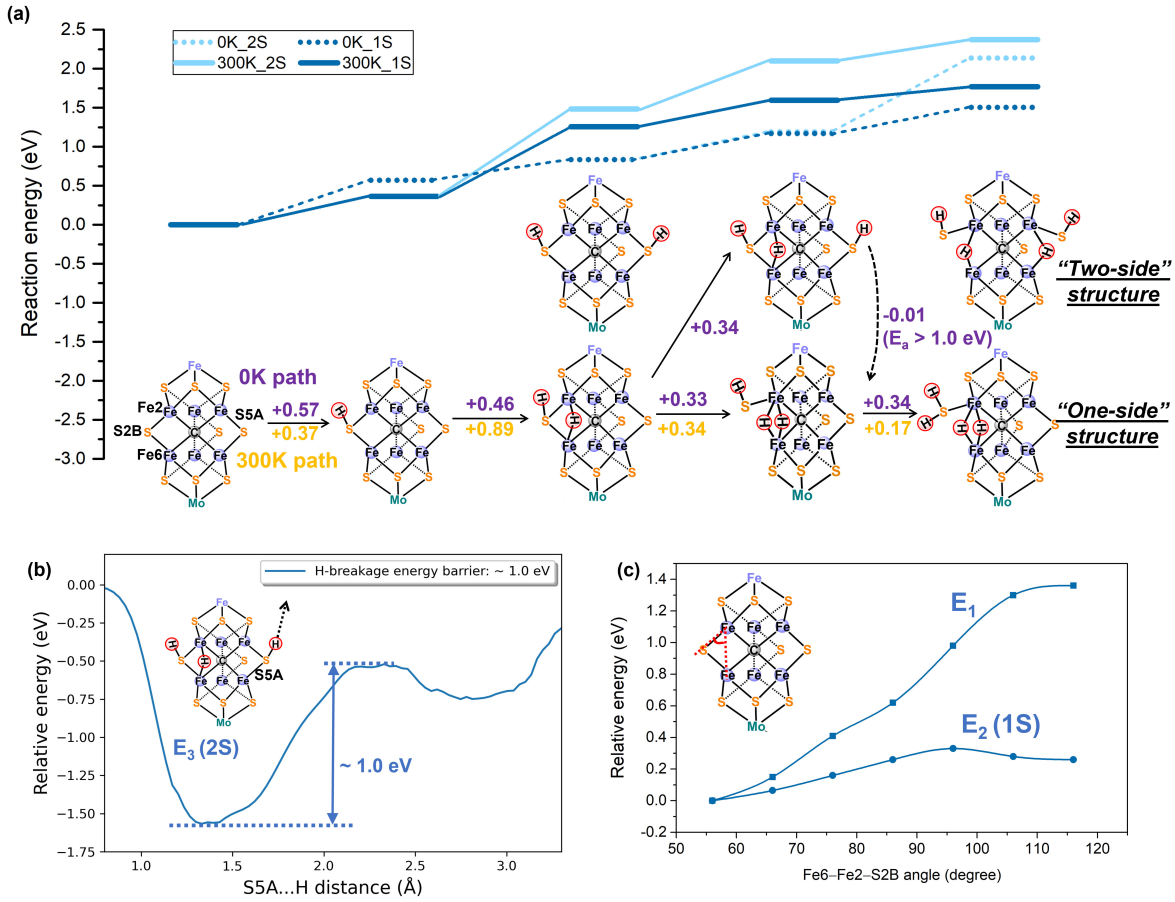

Figure 3: *Reaction path of the prerequisite H^+/e^- transfers.* (a) Energy profile of the H^+/e^- transfer path from $\mathbf{E}_0$ to $\mathbf{E}_4$ predicted by the BP86 functional at 0 K and 300 K. 2S and 1S structures are plotted in the first and second row, respectively. Energy differences at 300 K are calculated as the statistically averaged values. The minimum energy paths are highlighted in purple (0 K) and yellow (300 K). The dash lines represent the energy cost of 1S to 2S crossings. A similar set of results for the B97M-rV functional is provided in Figure S7. (b) One-dimensional free energy surface from a metadynamics simulation at 300 K, describing the H dissociation from the S5A site of the 2S structure at the $\mathbf{E}_3$ stage, indicating the energetic cost to cross from 2S to 1S is large. (c) Energy scans of Fe-S bond cleavage along the bond angle of Fe6-Fe2-S2B at $\mathbf{E}_1$ and $\mathbf{E}_2$ (1S) stage, respectively. We are unable to obtain the energy curve of the $\mathbf{E}_0$ due to the difficulty of SCF convergence, but the bond cleavage is estimated to be larger than 2.5 eV. The Fe-S bond cleavage becomes easier (less than 1.32 eV) when the S vertex is protonated. However, the Fe-S bond cleavage is facile to achieve after another proton transfers to the bridge of Fe2 and Fe6, with only a ∼0.35 eV barrier and ∼0.21 eV dissociation energy. This calculation is done at 0 K as we do not expect a qualitative change at 300 K due to the dramatic decrease of the dissociation energy in $\mathbf{E}_2$ compared with that in $\mathbf{E}_1$ ($>$ 1 eV).

Our computational results using both BP86 and B97M-rV methods consistently find the first protonation at $\mathbf{E}_1$ occurs at the bridged sulfide atoms between two Fe sites regardless of temperature as shown in Figure S4, consistent with experimental findings using K-edge EXAFS[81]. Proceeding to the $\mathbf{E}_2$ and $\mathbf{E}_3$ steps, of which the isomer relative energies are shown in Figure S5 and Figure S6, respectively, both DFT functionals at 0 K demonstrate a coexistence of 1S configuration with [Fe-H-Fe] formation and 2S configuration with protonation onto another bridging sulfide as shown in Figure 3a and Figure S7 at the level of BP86 and

B97M-rV functional, respectively. As depicted in Figure 3a and Figure S6, the energy difference between the 1S and 2S configurations within the $\mathbf{E}_3$ state is calculated to be lower than 0.01 eV, which is less than k_bT. As a result, there exist two potential pathways for the $\mathbf{E}_3$ transition: one through the 2S configuration and the other through the 1S configuration. Hoffman and coworkers[28,30] also found the same 2S structure for the $\mathbf{E}_4$ state. However, there must be an obligate side-crossing of hydrogen from S5A to the S2B site which would have to surmount a barrier of over 1 eV as demonstrated for the metadynamics simulation in Figure 3b for the $\mathbf{E}_3$ state; one would imagine the same large barrier would be present in the 4^{th} proton transfer of the $\mathbf{E}_4$ state.

On another hand, we determine that at 300 K both functionals exclusively prefer the 1S configuration path, which induces a more stable configuration of the bridging [Fe-H-Fe] due to the statistical thermal effects lowering the energy of one-side structure at room temperature. As a result of one-side structure, the formation of [Fe-H-Fe] for the $\mathbf{E}_2$ and $\mathbf{E}_3$ steps weakens the Fe←$(SH)^-$ bond (Figure 3c) so that the second hydride and H_2S formation at the $\mathbf{E}_4$ stage would completely open the Fe6 coordination site. The exposure of the Fe6 coordination site is energetically preferable for the N_2 adsorption. Notably, the temporary generation of the H_2S starting from $\mathbf{E}_4$ promotes the exposure of the iron coordination site but will not break the catalytic cycle because the H_2S will be consumed again during the hydrogenation reaction of dinitrogen. The complete nitrogenase environment contains residues that can hold H_2S via noncovalent interactions[48], and water chains (continuously transferring protons) connected through the homocitrate ligand can hydrolyze H_2S into H_3O^+ and HS^- that facilitates the binding to the holding site. This conclusion is also supported by a recent crystal of V-nitrogenase[43] that showed that an HS^- ion can bind in a holding site of the rearranged protein residue Gln-176 preventing its complete removal from the VMo-co.

Activation of N_2 and H_2 release

As determined above, the Fe2/Fe6 sites are completely exposed after the fourth proton transfer to FeMo-co, creating two bridged [Fe-H-Fe] bonds that are a favorable site for the adsorption of the N_2 molecule. Here, we use metadynamics within the collective coordinates that capture the adsorption and activation process in Figure 4. We find that N_2 absorbs onto the exposed Fe site of the $\mathbf{E}_4$ state via an $\mu_1 - \eta^1$ end-on mode (Figs. 4a and 4b), with a corresponding adsorption energy of -0.33 eV at 300 K (-0.40 eV at 0 K), and some small activation is present by bond elongation ∼0.05 Å (Figure 4c). Additionally, for the $\mu_1 - \eta^1$ end-on mode of the $\mathbf{E}_4$ state, the exposed Fe site with double hydrides for the 1S $\mathbf{E}_4$ configuration experiences an octahedral coordination field, which was proven to facilitate the doubly generated d_{xz} and d_{yz} orbitals of Fe that favors backbonding in the end-on N_2 ligand[82].

From the metadynamics simulation, we also determine an intermediate $\mathbf{E}_4\mathbf{N}_{2\_IM}$ state crossing a negligible free energy barrier of 0.06 eV from $\mathbf{E}_4\mathbf{N}_2$, which has a H_2-bound configuration that is consistent with recent photophysical experimental measurements[83]. From the intermediate state there is a low ∼ 0.18 eV energy barrier for release of H_2, which in turn stabilizes the adsorption of N_2 by more an 0.5 eV (implying a change from weak to strong binding) by allowing it to form an interaction with the two Fe atoms, defined as the $\mu_2 - \eta^2$ configuration (Figure 4b). The bond length is even elongated to be 1.20 Å, effectively coordinated to both Fe2 and Fe6 sites to facilitate the N_2 activation. Apparently, H_2 formation greatly enhances the N_2 binding from a weak to a stronger binding and further breaking its triple bond (see below), thus answering the long-standing unanswered question as to why H_2 formation is obligatory and how N_2 was activated[47]. Interestingly, this structure is in good agreement with the recent experimental observation of a synthetic [Mo_3S_4Fe] cube[15], which proposed that the N_2-reduction capability of Fe atoms is enhanced in a sulfur-rich environment. Overall, the $\mu_2 - \eta^2$ state is somewhere between end-on and side-on configurations, a point to which we return to in the next Section.

At both 0 and 300 K, the bond length of N_2 dramatically elongates by 0.11 Å in the bound $\mu_2 - \eta^2$

state relative to the free gaseous N_2 molecule, indicating the effective activation of N≡N to a formal N=N double bond according to the bond order (BO) indices in Figure 4b and 4c. Therefore, we conclude that the temporary dissociation of H_2S is necessary to fully expose the coordination site of Fe2/Fe6, increasing the N-Fe binding energy that in turn weakens the N_2 bond as illustrated by the longer N...N distance and shorter Fe...N distance. Although our results using the B97M-rV functional predicts a slightly different reaction sequence between the activation of N_2 and H_2 release (Figure S8), the outcome generated is the same, i.e. where we find that N_2 is efficiently activated based on the observed bond elongation by ∼0.09 Å.

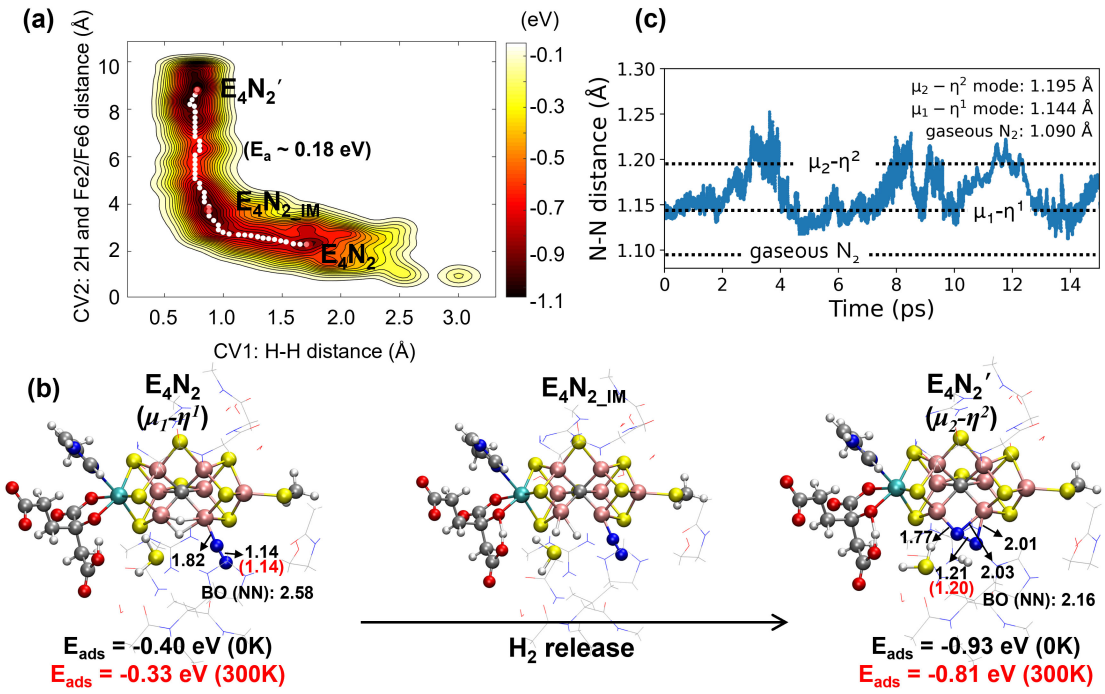

Figure 4: *N_2 adsorption and subsequent H_2 release using AIMD metadynamics simulations with the BP86 functional.* (a) a 15 ps metadynamics simulation, with at least five recrossings among the wells locating the main N_2 adsorption configurations and energetics. The minimum energy paths were calculated using the zero-temperature string method[84] and the activation barrier value is in parentheses. (b) The main configurations along the N_2 activation path: the end-on configuration of $\mathbf{E_4N_2}$ ($\mu_1 - \eta^1$), the intermediate state $\mathbf{E_4N_2}\_IM$, and the pseudo-side-on configuration of $\mathbf{E_4N_2'}$ ($\mu_2 - \eta^2$) as evaluated with metadynamics. N...N and Fe2/Fe6...N distances are listed, where red values are corresponding to 300 K results. Adsorption energies are calculated based on the total energy difference relative to $\mathbf{E_4}$ state under both 0 K (black) and 300 K (red). (c) The evolution of the N...N distance, showing N_2 activation compared to the gas phase. Wiberg bond order indices are listed here for a quantitative comparison.

In general, the H^+/e^- pairs (hydrogen atoms) are the source of the reducing ability, implying that the elimination of hydrogen atoms in the form of the H_2 molecule would weaken the reductive capacity of FeMo-cofactor. Hence our theoretical study does not support a postulation of reductive H_2 elimination[1,72]. Instead, we conclude that H_2 release eliminates the steric hindrance for N_2 chemical adsorption and activation. To further support these points, we performed chemical bonding analyses for the N_2 activated structures of $\mathbf{E_4N_2}$ and $\mathbf{E_4N_2'}$ predicted using the BP86 functional, illustrating the change of the electronic structure responsive to the adsorption conformations during the activation process. Wiberg bond order (BO)[85] indices and Weinhold effective atomic charges from natural population analysis (NPA)[86] are listed in Table S2. The formal triple bond of the free isolated N≡N molecule has a BO = 3.00, and it is further

effectively converted into a double bond (BO = 2.16, see also Figure 4) via electron back-donation from the adjacent Fe6 and Fe2 atoms. From the NPA charges, and despite the low electronegativity (EN) of iron (EN = 1.6 eV, while S and C have EN = 2.4 to 2.5 eV), the Fe atoms are negatively charged in the FeMo-co because of the formal C^{4-} unit at the center, which indicates the importance of the highly anionic carbon in the middle of a slightly deformed Fe6 octahedron to stabilize the geometrical skeleton[87] as well as to modulate electron transfers. The N...N π type bonding orbitals and its π^* antibonding counterparts are shown in Figure S9. From $\mathbf{E}_4\mathbf{N}_2$ to $\mathbf{E}_4\mathbf{N}_2'$, the back-donation of electrons from the 3d-shells is enhanced, coming from the two adjacent Fe sites, thus the total π^* antibonding occupation increases up to 0.5 e. This effectively activates the N≡N triple bond and changes the electronic charge density rearrangement to –N=N. According to Figure 5 and Figure S10, the steps of $\mathbf{E}_2$ and $\mathbf{E}_4\mathbf{N}_2'$ have similar relative energy, implying that it is a reversible process for the formation of H_2 and the adsorption of N_2 if there are no further protons and electrons transferred to the FeMo-cofactor to hydrogenate the N_2 to form ammonia, supporting the isoergic and thermodynamically reversible process of N_2 activation associated with H_2 release[83,88].

Hydrogenation steps after N_2 activation

A number of proposed mechanisms for N_2 reduction have been classified as dissociative and associative (alternating and distal) routes involving the end-on configuration[89], as well as the "enzymatic pathway" involving the side-on configuration.[90] Because there is some ambiguity of the pseudo side-on *vs* pseudo end-on configuration of the $\mathbf{E}_4\mathbf{N}_2'$ state, we must consider the full catalytic cycle by evaluating the $\mathbf{E}_5$ to $\mathbf{E}_8$ steps to best classify the N_2 reduction reaction of the nitrogenase enzyme.

Starting from the fully activated dinitrogen $\mathbf{E}_4\mathbf{N}_2'$ structure, the hydrogenation reaction pathway following the direct dissociation of N_2 was excluded, since a potential energy surface scan of the cleavage of the N=N double bond on the FeMo-co center yields a very high barrier of ∼1.72 eV. Instead, during the $\mathbf{E}_5$ step, the H^+/e^- pair is transferred to hydrogenate the activated -N=N- species at the terminal N atom, resulting in the formation of an -N=N-H intermediate. This process requires 0.58 eV of energy at 0 K, but is reduced to as low as 0.08 eV at room temperature, which is consistent with the associative mechanism.

The next hydrogenation step at $\mathbf{E}_6$ is preferable at 0 K temperature for both functionals, forming the -N=NH_2 intermediate consistent with the associative distal mechanism. However, it turns to be endothermic at 300 K when forming the distal configuration but the energy is still less than 0.2 eV. A potential energy scan of the alternating associative path of NH-NH_2 formation was evaluated as well, and was found to be unfavorable by +0.56 eV compared to the associative distal path forming -N-NH_3. The first NH_3 molecule is then spontaneously generated after one H^+/e^- pair transfer at $\mathbf{E}_7$ with a large amount of heat released, independent of functional or temperature.

Subsequently, in the $\mathbf{E}_7'$ state, the bridged N atom situated between the two Fe centers interacts with the H atom of the H_2S moiety. This interaction transforms the hydrogen bond into a stronger covalent N-H bond, resulting in a significant energy release (greater than 1 eV) and the cleavage of a HS^- species, with an energy barrier of 0.13 eV, as depicted in Figure 5b. The final H^+/e^- pair is transferred to the bridging N atom at $\mathbf{E}_8'$ stage, resulting in the formation of an -NH_2 intermediate species that is coordinated to the HS^- species. The temporarily released HS^- then returns to coordinate with the Fe active center, which is thermally stable but requires an energy barrier of 0.41 eV at 300 K.

In the final step, the H atom from the -SH ligand transfers to -NH_2 generating the second NH_3 molecule, and resetting the catalytic cycle after the final turnover, where H_2 and NH_3 are released with a product ratio of 1:2. We understand that using the half energy of H_2 as reference of hydrogen is not fully optimal, but it's the most convenient way to analyze such reactions. We believe that the hydrogen from Fe-protein and hydrolysis of ATP has a higher energy that would make the reaction more exothermic and feasible. However, based on the energy profile in Figure 5b, we find that once $\mathbf{E}_4$ is formed, the hydrogenation steps

from $\mathbf{E}_5$ to $\mathbf{E}_8$ exhibit almost complete exothermic behavior for each of these transformation steps.

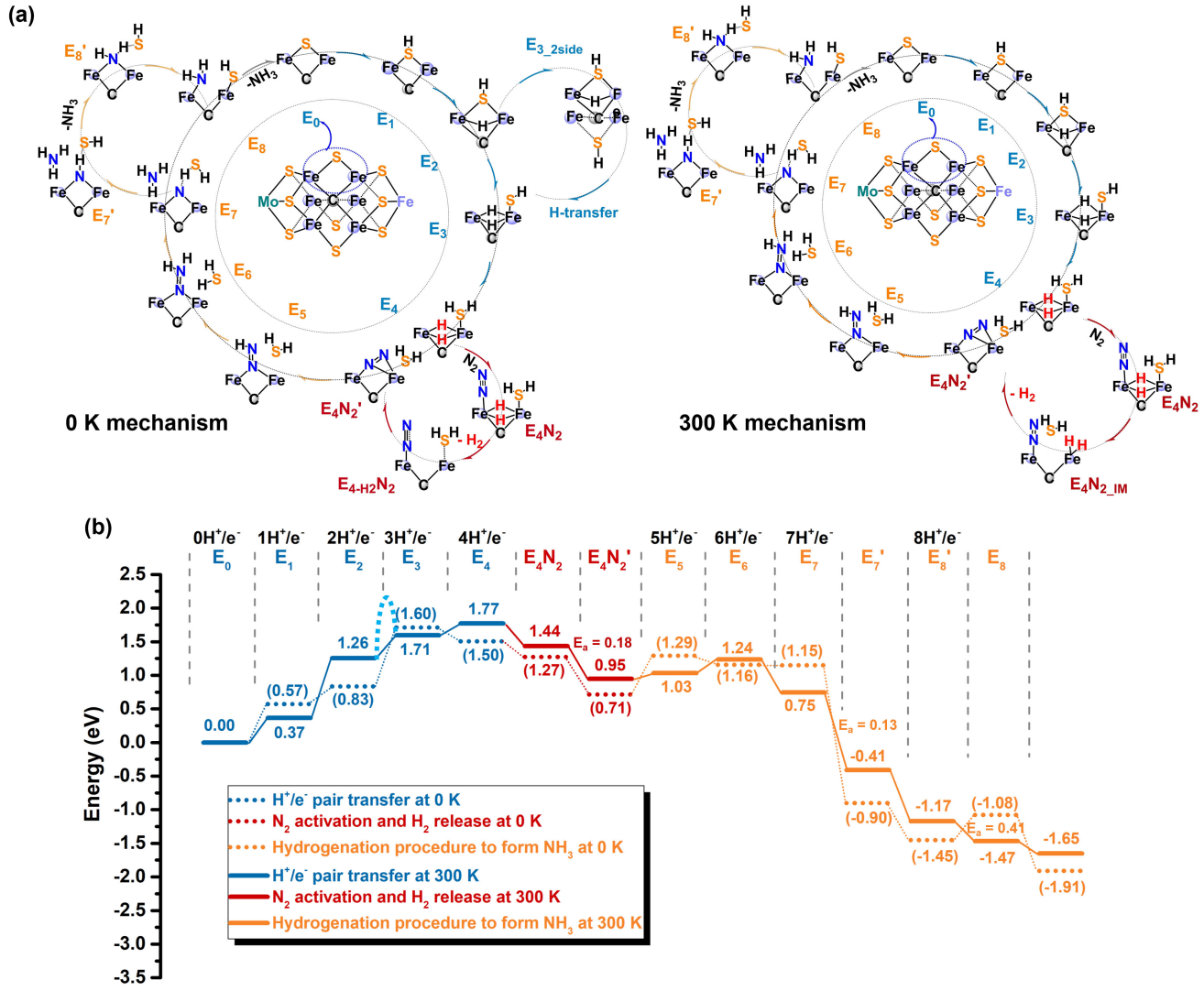

Figure 5: *The whole catalytic cycle of nitrogen fixation by nitrogenase.* (a) Active site geometries during the catalytic cycle at 0 K and 300 K obtained from the BP86 DFT functional. (b) The corresponding energy profiles at 0 K and 300 K for the three processes considered here: H^+/e^- pair transfers (blue), N_2 activation and H_2 release (red), and hydrogenation to form NH_3 (yellow). The energy of H^+/e^- is referred to a half energy of the H_2. The bent dotted curve implies the energetic cost of H-transfer to cross from r of the corresponding procedure under 300 K. Details of the reaction energy calculations are provided in the Models and methods section and supplemental information. The catalytic cycle from the B97M-rV functional is provided in Figure S10.

In summary, using two different levels of DFT methods, and more importantly, the statistical fluctuations of the FeMo-co reaction center at finite temperature, we have generated a well-supported mechanism over the entire catalytic cycle of nitrogenase. Overall the BP86 and B97M-rV support the same mechanism except the latter functional yields an extra step at the $\mathbf{E}_4$ stage, where N_2 can only be adsorbed after H_2 release, but nonetheless elongates the nitrogen bond by 0.09 Å. Regardless of DFT functional, thermal effects in particular yield a different result than found at 0 K by overwhelmingly favoring hydride adsorption

with a 1S configuration that (1) circumvents the side-crossing cost of H atom transfer of the 2S hydride adsorption, that is instead coexisting and inevitable with 1S adsorption at 0 K temperature, and (2) also weakening the Fe-SH bond to more readily form H_2S in $\mathbf{E}_4$. Finally, two such [Fe-H-Fe] hydrides formed in $\mathbf{E}_4$ leads to a complete exposure of the Fe6 coordination site for the subsequent N_2 adsorption regardless of DFT model.

Nonetheless, independent of the different levels of DFT methods applied, the "one-side" reaction pathway provides a compelling view of not only N_2 adsorption but a chemically activated N_2 bond. In particular, it predicts an N_2 pre-adsorption mode from the $\mu_1 - \eta^1$ state which weakens the N≡N bond, and after H_2 release is subsequently activated through a highly exothermic $\mu_2 - \eta^2$ bound state that induces a chemical change, reducing the bond order to near 2.2 as the bond length increases up to 1.20 Å. The creation of the H_2S molecule is never observed in the LT mechanism as it can be hydrolyzed into HS^- and H^+ via a water microenvironment, and held in a holding site of the rearranged protein residue Gln-176 to prevent its complete removal from the FeMo-co[43]. Once the vital step of N_2 activation is fulfilled, the following hydrogenation steps from $\mathbf{E}_5$ to $\mathbf{E}_8$ come about naturally to form two NH_3 molecules, while demonstrating a highly exothermic process at the completion of the catalytic cycle.

This work provides a thorough catalytic mechanism of nitrogenase upon full consideration of the detailed fluctuations of a complete statistical mechanical ensemble: the accumulation of H^+/e^- pairs on the S and Fe sites of FeMo-co for ($\mathbf{E}_0$ to $\mathbf{E}_4$), the necessity of H_2 formation to promote not just N_2 weak binding but its chemical activation, and the subsequent hydrogenation of the activated N_2 to form NH_3 ($\mathbf{E}_5$ to $\mathbf{E}_8$). We believe that further enlightening the catalytic pathway in nature's best catalysts is often the best approach to improving synthetic catalysts[55,91], including those that aim to optimize other nitrogen fixation reactions.

EXPERIMENTAL PROCEDURES

Resource availability

Lead contact

Further information and requests for resources should be informed to and will be fulfilled by the lead contact, Teresa Head-Gordon (thg@berkeley.edu).

Materials availability

This study did not generate any new unique reagent or material.

Data and code availability

Coordinates of optimized intermediates along the entire the catalytic circle with cluster model at B97M-rV and BP86 levels under the temperature of 0 K are included in the supplementary information as Data_S2. As well as the supplementary geometrical data, the published article includes all datasets generated or analyzed during this study.

Models and methods

Based on the FeMo-co cluster model shown in Figure 2a, we first optimized the geometrical structures with implicit solvent approximated by the COSMO method. Pure GGA-BP86[27,92] and dispersion corrected meta-GGA functional B97M-rV[66] were employed, with optimized small-core GTH pseudopotential[93–95] and the corresponding TZVP MOLOPT basis sets[96] as implemented in CP2K software[97,98]. The quality of new pseudopotentials for describing the catalytic behavior of first-row transition metals have been demonstrated in several recent papers[99–103]. In all calculations, we used 5 grids for the integral accuracy and the truncated α-C atoms were fixed during the optimization and molecular dynamic simulations. During the geometry optimizations, the convergence criteria were set as 3×10^{-3} bohr for atomic displacements and 4.5×10^{-4} hartree/bohr for the forces. The reaction energies and activation energy barriers in the main text are all obtained from CP2K package.

The electronic structure and spin state determination of $\mathbf{E}_0$, and chemical bonding analyses were performed with the Gaussian 09 D.01 software package (G09)[104] for the BP86 functional along with 6-311+G* basis sets for C, N, O, and H, and 6-311+G(2d,p) for S atom[105]. In terms of the heavier elements, effective core pseudo-potentials (ECP)[106] were used with ECP10MDF for Fe, and ECP28MWB for Mo, together with triple-zeta basis sets[107]. The broken-symmetry (BS) method was also used to elucidate the electronic structures of three configurations of BS7 (BS7-346, BS7-235, BS7-247), based on which we found the three states are almost degenerate with the energy difference of less than 0.05 eV and BS7-346 was the preferable one. The stability of the single-determinant Kohn-Sham-DFT (KS-DFT) wave function was evaluated to ensure that the obtained KS-DFT wave function corresponds to an energy minimum and not a saddle point at low spin states[108,109]. For the transferability between different packages, we also compared the results generated from G09 with the ones from CP2K with the same BP86 functional regarding the $\mathbf{E}_0$ geometry (Table S1) and the total reaction pathway at 0 K, where they resemble with each other quite well rationalizing the model of the system. Even though the reaction energy is slightly different, the qualitive conclusion remains unchanged.

Ab initio molecular dynamic simulations

To calculate the adsorption energies of each state at 300 K, we performed AIMD simulations with the timestep of 0.5 fs in the NVT ensemble with a cubic box (a = b = c = 30 Å). Statistical average values were collected over 5 ps with 1 ps equilibration, where the convergence was determined by the energy fluctuation less than 0.01 eV per atom. By utilizing the ensemble-averaged method to consider the anharmonicity[54] on top of a long-simulation trajectories, the corresponding time-averaged adsorption energy is calculated as per Eq. (2), where the energies are potential energies with consideration of anharmonic contributions through finite temperature simulations.

$$\langle \triangle E_{ads,n} \rangle_{300K} = \langle E_n \rangle_{300K} - \langle E_{n-1} \rangle_{300K} - \frac{1}{2} \langle E_{H_2/N_2} \rangle_{300K} \tag{2}$$

Free energy calculations

To calculate free energy barriers, we performed well-tempered single walker metadynamic simulations[110,111] for as long as 15 ps using the CP2K package. Two collective variables (CVs) were picked to reduce the dimension of reaction space: (i) the distance between two bridged H atoms of [Fe-H-Fe] and (ii) the distance between the center of two bridged H atoms and the center of Fe2 and Fe6 sites. A wall with the position at 5 angstrom was set for the second collective variable to avoid the complete dissociation of H_2 which is hard to make the reaction backward to sufficiently sample the wells on free energy surface. In the metadynamic calculation, Gaussian functions with 0.002 Hartree height were deposited at least every 30 steps to introduce a bias to introduce a bias in reaction space. The minimum energy path was obtained using the zero-temperature string method proposed by Maragliano and co-workers[84]. We employed the forward Euler approach to capture the overdamped dynamic properties of the string snapshots in the CV 2D space as Eqs. 3 and 4:

$$(CV_1)_i = (CV_1)_{i+1} - h \bigtriangledown_{CV_1} F \tag{3}$$

$$(CV_2)_i = (CV_2)_{i+1} - h \bigtriangledown_{CV_2} F \tag{4}$$

where h = 1×10^{-3}, F is corresponding to the free energy surface. The algorithm was performed in Matlab package using a 50 point string joining the local minima and 2000 optimization steps. The convergence is set to be 1×10^{-5}. Further details and discussion of the computational models are provided in the supplemental information.

ACKNOWLEDGEMENTS

T.H-G and W.L.L. thank the CPIMS program, Office of Science, Office of Basic Energy Sciences, Chemical Sciences Division of the U.S. Department of Energy under Contract DE-AC02-05CH11231 for support. This work used computational resources provided by the National Energy Research Scientific Computing Center (NERSC), a U.S. Department of Energy Office of Science User. Facility operated under Contract DE-AC02-05CH11231. J.L and Y.L are supported by the National Natural Science Foundation of China (Grant No. 22033005), the National Key R&D Project (Grant Nos. 2022YFA1503900, 2022YFA1503000), and the Guangdong Provincial Key Laboratory of Catalysis (No. 2020B121201002).

AUTHOR CONTRIBUTIONS

W.L.L., Y.L. and T.H.G. designed the project. W.L.L. carried out the AIMD simulation, metadynamic calculation and performed bonding analyses. Y.L. designed the reaction paths and mechanism, and determined the electronic structure and the scan curve calculation with the help of J.L. All authors discussed the results and made comments and edits to the manuscript.

DECLARATION OF INTERESTS

The authors declare no competing interests.

SUPPLEMENTAL INFORMATION

Data S2: Coordinates of optimized intermediates along the entire the catalytic cycle.

References

[1] Hoffman, B. M., Lukoyanov, D., Yang, Z.-Y., Dean, D. R. and Seefeldt, L. C. (2014). Mechanism of nitrogen fixation by nitrogenase: The next stage. Chem. Rev. *114*, 4041–4062.

[2] Dance, I. (2020). Computational investigations of the chemical mechanism of the enzyme nitrogenase. ChemBioChem. *21*, 1671–1709.

[3] Van Stappen, C., Decamps, L., Cutsail, G. E., Bjornsson, R., Henthorn, J. T., Birrell, J. A. and DeBeer, S. (2020). The spectroscopy of nitrogenases. Chem. Rev. *120*, 5005–5081.

[4] Tanifuji, K. and Ohki, Y. (2020). Metal–sulfur compounds in N_2 reduction and nitrogenase-related chemistry. Chem. Rev. *120*, 5194–5251.

[5] Seefeldt, L. C., Yang, Z. Y., Lukoyanov, D. A., Harris, D. F., Dean, D. R., Raugei, S. and Hoffman, B. M. (2020). Reduction of Substrates by Nitrogenases. Chem. Rev. *120*, 5082–5106.

[6] Jia, H.-P. and Quadrelli, E. A. (2014). Mechanistic aspects of dinitrogen cleavage and hydrogenation to produce ammonia in catalysis and organometallic chemistry: relevance of metal hydride bonds and dihydrogen. Chem. Soc. Rev. *43*, 547–564.

[7] Spatzal, T., Aksoyoglu, M., Zhang, L., Andrade, S. L. A., Schleicher, E., Weber, S., Rees, D. C. and Einsle, O. (2011). Evidence for interstitial carbon in nitrogenase FeMo cofactor. Science *334*, 940–940.

[8] Simpson, F. B. and Burris, R. H. (1984). A nitrogen pressure of 50 atmospheres does not prevent evolution of hydrogen by nitrogenase. Science *224*, 1095–1097.

[9] Eady, R. R. (1996). Structure Function Relationships of Alternative Nitrogenases. Chem. Rev. *96*, 3013–3030.

[10] Hu, Y., Lee, C. C. and Ribbe, M. W. (2012). Vanadium nitrogenase: A two-hit wonder? Dalton Trans. *41*, 1118–1127.

[11] Mcglynn, S., Boyd, E., Peters, J. and Orphan, V. (2013). Classifying the metal dependence of uncharacterized nitrogenases. Front. Microbiol. *3*.

[12] Betancourt, D. A., Loveless, T. M., Brown, J. W. and Bishop, P. E. (2008). Characterization of Diazotrophs Containing Mo-Independent Nitrogenases, Isolated from Diverse Natural Environments. Appl. Environ. Microbiol. *74*, 3471–3480.

[13] Boyd, E. S., Costas, A. M. G., Hamilton, T. L., Mus, F. and Peters, J. W. (2015). Evolution of Molybdenum Nitrogenase during the Transition from Anaerobic to Aerobic Metabolism. J. Bacteriol. *197*, 1690–1699.

[14] Bishop, P. E., Jarlenski, D. M. and Hetherington, D. R. (1980). Evidence for an alternative nitrogen fixation system in Azotobacter vinelandii. Proc. Natl. Acad. Sci. U.S.A. *77*, 7342–7346.

[15] Ohki, Y. *et al.* (2022). Nitrogen reduction by the Fe sites of synthetic Mo_3S_4Fe cubes. Nature *7917*, 86–90.

[16] Rohde, M., Christian Trncik, D. S., Gerhardt, S. and Einsle, O. (2018). Crystal structure of VnfH, the iron protein component of vanadium nitrogenase. J. Biol. Inorg. Chem. *23*, 1049–1056.

[17] Dance, I. (2015). The pathway for serial proton supply to the active site of nitrogenase: enhanced density functional modeling of the Grotthuss mechanism. Dalton Trans. *44*, 18167–18186.

[18] Rutledge, H. L. and Tezcan, F. A. (2020). Electron transfer in nitrogenase. Chem. Rev. *120*, 5158–5193.

[19] Einsle, O. and Rees, D. C. (2020). Structural enzymology of nitrogenase enzymes. Chem. Rev. *120*, 4969–5004.

[20] Kang, W., Lee, C. C., Jasniewski, A. J., Ribbe, M. W. and Hu, Y. (2020). Structural evidence for a dynamic metallocofactor during N_2 reduction by mo-nitrogenase. Science *368*, 1381–1385.

[21] Peters, J. W., Einsle, O., Dean, D. R., DeBeer, S., Hoffman, B. M., Holland, P. L. and Seefeldt, L. C. (2021). Comment on "Structural evidence for a dynamic metallocofactor during N_2 reduction by Mo-nitrogenase";. Science *371*, eabe5481.

[22] Bergmann, J., Oksanen, E. and Ryde, U. (2021). Critical evaluation of a crystal structure of nitrogenase with bound N_2 ligands. JBIC J. Biol. Inorg. Chem. *26*, 341–353.

[23] Bjornsson, R., Lima, F. A., Spatzal, T., Weyhermüller, T., Glatzel, P., Bill, E., Einsle, O., Neese, F. and DeBeer, S. (2014). Identification of a spin-coupled Mo(III) in the nitrogenase iron–molybdenum cofactor. Chem. Sci. *5*, 3096–3103.

[24] Bjornsson, R., Neese, F. and DeBeer, S. (2017). Revisiting the mössbauer isomer shifts of the FeMoco cluster of nitrogenase and the cofactor charge. Inorg. Chem. *56*, 1470–1477.

[25] Spiller, N., Bjornsson, R., DeBeer, S. and Neese, F. (2021). Carbon Monoxide Binding to the Iron–Molybdenum Cofactor of Nitrogenase: a Detailed Quantum Mechanics/Molecular Mechanics Investigation. Inorg. Chem. *60*, 18031–18047.

[26] Hohenberg, P. and Kohn, W. (1964). Inhomogeneous Electron Gas. Phys. Rev. *136*, B864–B871.

[27] Becke, A. D. (1988). Density-functional exchange-energy approximation with correct asymptotic behavior. Phys. Rev. A *38*, 3098–3100.

[28] Raugei, S., Seefeldt, L. C. and Hoffman, B. M. (2018). Critical computational analysis illuminates the reductive-elimination mechanism that activates nitrogenase for N_2 reduction. Proc. Natl. Acad. Sci. U.S.A. *115*, E10521–E10530.

[29] Hoeke, V., Tociu, L., Case, D. A., Seefeldt, L. C., Raugei, S. and Hoffman, B. M. (2019). High-Resolution ENDOR Spectroscopy Combined with Quantum Chemical Calculations Reveals the Structure of Nitrogenase Janus Intermediate E_4(4H). J. Am. Chem. Soc. *141*, 11984–11996.

[30] Lukoyanov, D. A., Yang, Z.-Y., Dean, D. R., Seefeldt, L. C., Raugei, S. and Hoffman, B. M. (2020). Electron Redistribution within the Nitrogenase Active Site FeMo-Cofactor During Reductive Elimination of H_2 to Achieve N_2 Triple-Bond Activation. J. Am. Chem. Soc. *142*, 21679–21690.

[31] Siegbahn, P. E. M. and Blomberg, M. R. A. (2018). A Systematic DFT Approach for Studying Mechanisms of Redox Active Enzymes. Front. Chem. *6*.

[32] Siegbahn, P. E. M. (2019). The mechanism for nitrogenase including all steps. Phys. Chem. Chem. Phys. *21*, 15747–15759.

[33] Cao, L. and Ryde, U. (2020). Putative reaction mechanism of nitrogenase after dissociation of a sulfide ligand. J. Catal. *391*, 247–259.

[34] Cao, L. and Ryde, U. (2020). N_2H_2 binding to the nitrogenase FeMo cluster studied by QM/MM methods. BIC J. Biol. Inorg. Chem. *25*, 521–540.

[35] Jiang, H., Svensson, O. K. G., Cao, L. and Ryde, U. (2022). Proton Transfer Pathways in Nitrogenase with and without Dissociated S2B. Angew. Chem. Int. Ed. *134*, e202208.

[36] Jiang, H. and Ryde, U. (2022). Thermodynamically favourable states in the reaction of nitrogenase without dissociation of any sulfide ligand. Chem. Eur. J. *28*, e202103933.

[37] Jiang, H., Svensson, O. K. G. and Ryde, U. (2023). Quantum mechanical calculations of redox potentials of the metal clusters in nitrogenase. Molecules *28*.

[38] Kästner, J. and Blöchl, P. E. (2007). Ammonia production at the FeMo cofactor of nitrogenase: Results from Density Functional Theory. J. Am. Chem. Soc. *129*, 2998–3006.

[39] Spatzal, T., Perez, K. A., Einsle, O., Howard, J. B. and Rees, D. C. (2014). Ligand binding to the FeMo-cofactor: Structures of CO-bound and reactivated nitrogenase. Science *345*, 1620–1623.

[40] Rohde, M., Grunau, K. and Einsle, O. (2020). CO Binding to the FeV Cofactor of CO-Reducing Vanadium Nitrogenase at Atomic Resolution. Angew. Chem. Int. Ed. *59*, 23626–23630.

[41] Benediktsson, B., Thorhallsson, A. T. and Bjornsson, R. (2018). QM/MM calculations reveal a bridging hydroxo group in a vanadium nitrogenase crystal structure. Chem. Commun. *54*, 7310–7313.

[42] Spatzal, T., Perez, K. A., Howard, J. B. and Rees, D. C. (2015). Catalysis-dependent selenium incorporation and migration in the nitrogenase active site iron-molybdenum cofactor. eLife *4*, e11620.

[43] Sippel, D., Rohde, M., Netzer, J., Trncik, C., Gies, J., Grunau, K., Djurdjevic, I., Decamps, L., Andrade, S. L. A. and Einsle, O. (2018). A bound reaction intermediate sheds light on the mechanism of nitrogenase. Science *359*, 1484–1489.

[44] Henthorn, J. T., Arias, R. J., Koroidov, S., Kroll, T., Sokaras, D., Bergmann, U., Rees, D. C. and DeBeer, S. (2019). Localized Electronic Structure of Nitrogenase FeMoco Revealed by Selenium K-Edge High Resolution X-ray Absorption Spectroscopy. J. Am. Chem. Soc. *141*, 13676–13688.

[45] Bukas, V. J. and Nørskov, J. K. A Molecular-Level Mechanism of the Biological N_2 Fixation. ChemRxiv. doi: 10.26434/chemrxiv.10029224.v1 .

[46] Li, Y., Li, W.-L., Liu, J.-C., Lu, J.-B., Schwarz, W. H. E. and Moskaleva, L. V. (2020). H_2 formation holds the key to opening the Fe coordination sites of nitrogenase FeMo-cofactor for dinitrogen activation. ChemRxiv. 10.26434/chemrxiv.13015994.v1 .

[47] Thorhallsson, A. T., Benediktsson, B. and Bjornsson, R. (2019). A model for dinitrogen binding in the E_4 state of nitrogenase. Chem. Sci. *10*, 11110–11124.

[48] Dance, I. (2019). How feasible is the reversible S-dissociation mechanism for the activation of FeMo-co, the catalytic site of nitrogenase? Dalton Trans. *48*, 1251–1262.

[49] Dance, I. (2022). Understanding the tethered unhooking and rehooking of S2B in the reaction domain of FeMo-co, the active site of nitrogenase. Dalton Trans. *51*, 15538–15554.

[50] Dance, I. (2023). The binding of reducible N2 in the reaction domain of nitrogenase. Dalton Trans. *52*, 2013–2026.

[51] Thorhallsson, A. T. and Bjornsson, R. (2021). The E_2 state of FeMoco: Hydride Formation versus Fe Reduction and a Mechanism for H_2 Evolution. Chem.-Eur. J. *27*, 16788–16800.

[52] Jiang, H., Svensson, O. K. G. and Ryde, U. (2022). QM/MM Study of Partial Dissociation of S2B for the E2 Intermediate of Nitrogenase. Inorg. Chem. *61*, 18067–18076.

[53] Fraser, J. S., van den Bedem, H., Samelson, A. J., Lang, P. T., Holton, J. M., Echols, N. and Alber, T. (2011). Accessing protein conformational ensembles using room-temperature X-ray crystallography. Proc. Natl. Acad. Sci. U.S.A. *108*, 16247–16252.

[54] Li, W.-L., Lininger, C. N., Chen, K., Vaissier Welborn, V., Rossomme, E., Bell, A. T., Head-Gordon, M. and Head-Gordon, T. (2021). Critical Role of Thermal Fluctuations for CO Binding on Electrocatalytic Metal Surfaces. JACS Au *1*, 1708–1718.

[55] Li, W.-L. and Head-Gordon, T. (2021). Catalytic Principles from Natural Enzymes and Translational Design Strategies for Synthetic Catalysts. ACS Cent. Sci. *7*, 72–80.

[56] Welborn, V. V. and Head-Gordon, T. (2019). Fluctuations of Electric Fields in the Active Site of the Enzyme Ketosteroid Isomerase. J. Am. Chem. Soc. *141*, 12487–12492.

[57] Hammes-Schiffer, S. (2002). Impact of Enzyme Motion on Activity. Biochemistry *41*, 13335–13343.

[58] Bhowmick, A. and Head-Gordon, T. (2015). A Monte Carlo Method for Generating Side Chain Structural Ensembles. Structure *23*, 44–55.

[59] Offenbacher, A. R. *et al.* (2017). Hydrogen–Deuterium Exchange of Lipoxygenase Uncovers a Relationship between Distal, Solvent Exposed Protein Motions and the Thermal Activation Barrier for Catalytic Proton-Coupled Electron Tunneling. ACS Cent. Sci. *3*, 570–579.

[60] Yoo, S. J., Angove, H. C., Papaefthymiou, V., Burgess, B. K. and Münck, E. (2000). Mössbauer study of the MoFe protein of nitrogenase from Azotobacter vinelandii Using selective ^{57}Fe enrichment of the M-Centers. J. Am. Chem. Soc. *122*, 4926–4936.

[61] True, A. E., Nelson, M. J., Venters, R. A., Orme-Johnson, W. H. and Hoffman, B. M. (1988). Iron-57 hyperfine coupling tensors of the FeMo cluster in Azotobacter vinelandii MoFe protein: determination by polycrystalline ENDOR spectroscopy. J. Am. Chem. Soc. *110*, 1935–1943.

[62] Spatzal, T., Schlesier, J., Burger, E.-M., Sippel, D., Zhang, L., Andrade, S. L., Rees, D. C. and Einsle, O. (2016). Nitrogenase femoco investigated by spatially resolved anomalous dispersion refinement. Nat. Commun. *7*, 10902.

[63] Cao, L., Caldararu, O. and Ryde, U. (2017). Protonation States of Homocitrate and Nearby Residues in Nitrogenase Studied by Computational Methods and Quantum Refinement. J. Phys. Chem. B *121*, 8242–8262.

[64] Huynh, B., Henzl, M., Christner, J., Zimmermann, R., Orme-Johnson, W. and Münck, E. (1980). Nitrogenase XII. Mössbauer studies of the MoFe protein from Clostridium pasteurianum W5. Biochimica et Biophysica Acta (BBA) - Protein Structure *623*, 124–138.

[65] Mardirossian, N. and Head-Gordon, M. (2015). Mapping the genome of meta-generalized gradient approximation density functionals: The search for B97M-V. J. Chem. Phys. *142*, 074111.

[66] Mardirossian, N., Ruiz Pestana, L., Womack, J. C., Skylaris, C.-K., Head-Gordon, T. and Head-Gordon, M. (2017). Use of the rVV10 Nonlocal Correlation Functional in the B97M-V Density Functional: Defining B97M-rV and Related Functionals. J. Phys. Chem. Lett. *8*, 35–40.

[67] Ruiz Pestana, L., Mardirossian, N., Head-Gordon, M. and Head-Gordon, T. (2017). Ab initio molecular dynamics simulations of liquid water using high quality meta-GGA functionals. Chem. Sci. *8*, 3554–3565.

[68] Mardirossian, N. and Head-Gordon, M. (2017). Thirty years of density functional theory in computational chemistry: an overview and extensive assessment of 200 density functionals. Mol. Phys. *115*, 2315–2372.

[69] Lininger, C. N., Gauthier, J. A., Li, W.-L., Rossomme, E., Welborn, V. V., Lin, Z., Head-Gordon, T., Head-Gordon, M. and Bell, A. T. (2021). Challenges for density functional theory: calculation of CO adsorption on electrocatalytically relevant metals. Phys. Chem. Chem. Phys. *23*, 9394–9406.

[70] Burgess, B. K. and Lowe, D. J. (1996). Mechanism of molybdenum nitrogenase. Chem. Rev. *96*, 2983–3012.

[71] Wilson, P., Nyborg, A. and Watt, G. (2001). Duplication and extension of the Thorneley and Lowe kinetic model for Klebsiella pneumoniae nitrogenase catalysis using a mathematica software platform. Biophys. Chem. *91*, 281–304.

[72] Hoffman, B. M., Lukoyanov, D., Dean, D. R. and Seefeldt, L. C. (2013). Nitrogenase: A Draft Mechanism. Acc. Chem. Res. *46*, 587–595.

[73] Cao, L., Caldararu, O. and Ryde, U. (2018). Protonation and Reduction of the FeMo Cluster in Nitrogenase Studied by Quantum Mechanics/Molecular Mechanics (QM/MM) Calculations. J. Chem. Theory Comput. *14*, 6653–6678.

[74] Igarashi, R. Y., Laryukhin, M., Dos Santos, P. C., Lee, H.-I., Dean, D. R., Seefeldt, L. C. and Hoffman, B. M. (2005). Trapping H-Bound to the Nitrogenase FeMo-Cofactor Active Site during H_2 Evolution: Characterization by ENDOR Spectroscopy. J. Am. Chem. Soc. *127*, 6231–6241.

[75] Lukoyanov, D., Yang, Z.-Y., Dean, D. R., Seefeldt, L. C. and Hoffman, B. M. (2010). Is Mo Involved in Hydride Binding by the Four-Electron Reduced (E_4) Intermediate of the Nitrogenase MoFe Protein? J. Am. Chem. Soc. *132*, 2526–2527.

[76] Benton, P. M. C., Laryukhin, M., Mayer, S. M., Hoffman, B. M., Dean, D. R. and Seefeldt, L. C. (2003). Localization of a Substrate Binding Site on the FeMo-Cofactor in Nitrogenase: Trapping Propargyl Alcohol with an alpha-70-Substituted MoFe Protein. Biochem. *42*, 9102–9109.

[77] Lee, H.-I., Igarashi, R. Y., Laryukhin, M., Doan, P. E., Dos Santos, P. C., Dean, D. R., Seefeldt, L. C. and Hoffman, B. M. (2004). An Organometallic Intermediate during Alkyne Reduction by Nitrogenase. J. Am. Chem. Soc. *126*, 9563–9569.

[78] Seefeldt, L. C., Hoffman, B. M. and Dean, D. R. (2009). Mechanism of Mo-dependent nitrogenase. Annu. Rev. Biochem. *78*, 701–722.

[79] Cao, L. and Ryde, U. (2019). Extremely large differences in DFT energies for nitrogenase models. Phys. Chem. Chem. Phys. *21*, 2480–2488.

[80] Cao, L. and Ryde, U. (2020). What is the structure of the E_4 intermediate in nitrogenase? J. Chem. Theory Comput. *16*, 1936–1952.

[81] Van Stappen, C., Thorhallsson, A. T., Decamps, L., Bjornsson, R. and DeBeer, S. (2019). Resolving the structure of the E1 state of Mo nitrogenase through Mo and Fe K-edge EXAFS and QM/MM calculations. Chem. Sci. *10*, 9807–9821.

[82] Pang, Y. and Bjornsson, R. (2023). Understanding the Electronic Structure Basis for N2 Binding to FeMoco: A Systematic Quantum Mechanics/Molecular Mechanics Investigation. Inorg. Chem. *62*, 5357–5375.

[83] Lukoyanov, D., Khadka, N., Dean, D. R., Raugei, S., Seefeldt, L. C. and Hoffman, B. M. (2017). Photoinduced Reductive Elimination of H_2 from the Nitrogenase Dihydride (Janus) State Involves a FeMo-cofactor-H_2 Intermediate. Inorg. Chem. *56*, 2233–2240.

[84] Maragliano, L., Fischer, A., Vanden-Eijnden, E. and Ciccotti, G. (2006). String method in collective variables: Minimum free energy paths and isocommittor surfaces. J. Chem. Phys. *125*, 024106.

[85] Wiberg, K. (1968). Application of the pople-santry-segal CNDO method to the cyclopropylcarbinyl and cyclobutyl cation and to bicyclobutane. Tetrahedron *24*, 1083–1096.

[86] Reed, A. E., Weinstock, R. B. and Weinhold, F. (1985). Natural population analysis. J. Chem. Phys. *83*, 735–746.

[87] Grunenberg, J. (2017). The Interstitial Carbon of the Nitrogenase FeMo Cofactor is Far Better Stabilized than Previously Assumed. Angew. Chem. Int. Ed. *56*, 7288–7291.

[88] Lukoyanov, D., Khadka, N., Yang, Z.-Y., Dean, D. R., Seefeldt, L. C. and Hoffman, B. M. (2016). Reductive Elimination of H2 Activates Nitrogenase to Reduce the NN Triple Bond: Characterization of the E4(4H) Janus Intermediate in Wild Type Enzyme. J. Am. Chem. Soc. *138*, 10674–10683.

[89] Cui, X., Tang, C. and Zhang, Q. (2018). A Review of Electrocatalytic Reduction of Dinitrogen to Ammonia under Ambient Conditions. Adv. Energy Mater. *8*, 1800369.

[90] Li, X.-F., Li, Q.-K., Cheng, J., Liu, L., Yan, Q., Wu, Y., Zhang, X.-H., Wang, Z.-Y., Qiu, Q. and Luo, Y. (2016). Conversion of Dinitrogen to Ammonia by FeN_3-Embedded Graphene. J. Am. Chem. Soc. *138*, 8706–8709. PMID: 27383680.

[91] Welborn, V. V., Li, W.-L. and Head-Gordon, T. (2020). Interplay of water and a supramolecular capsule for catalysis of reductive elimination reaction from gold. Nature Commun. *11*, 415.

[92] Perdew, J. P. (1986). Density-functional approximation for the correlation energy of the inhomogeneous electron gas. Phys. Rev. B *33*, 8822–8824.

[93] Goedecker, S., Teter, M. and Hutter, J. (1996). Separable dual-space Gaussian pseudopotentials. Phys. Rev. B *54*, 1703–1710.

[94] Hartwigsen, C., Goedecker, S. and Hutter, J. (1998). Relativistic separable dual-space Gaussian pseudopotentials from H to Rn. Phys. Rev. B *58*, 3641–3662.

[95] Li, W.-L., Chen, K., Rossomme, E., Head-Gordon, M. and Head-Gordon, T. (2021). Optimized Pseudopotentials and Basis Sets for Semiempirical Density Functional Theory for Electrocatalysis Applications. J. Phys. Chem. Lett. *12*, 10304–10309.

[96] VandeVondele, J. and Hutter, J. (2007). Gaussian basis sets for accurate calculations on molecular systems in gas and condensed phases. J. Chem. Phys. *127*, 114105.

[97] VandeVondele, J., Krack, M., Mohamed, F., Parrinello, M., Chassaing, T. and Hutter, J. (2005). Quickstep: fast and accurate density functional calculations using a mixed Gaussian and plane waves approach. Comput. Phys. Commun. *167*, 103–128.

[98] Hutter, J., Iannuzzi, M., Schiffmann, F. and VandeVondele, J. (2014). CP2K: atomistic simulations of condensed matter systems. WIREs Comput. Mol. Sci. *4*, 15–25.

[99] Chen, X., Ge, H. and Yang, X. (2017). Newly designed manganese and cobalt complexes with pendant amines for the hydrogenation of CO2 to methanol: a DFT study. Catal. Sci. Technol. *7*, 348–355.

[100] De Luca, L., Passera, A. and Mezzetti, A. (2019). Asymmetric Transfer Hydrogenation with a Bifunctional Iron(II) Hydride: Experiment Meets Computation. J. Am. Chem. Soc. *141*, 2545–2556.

[101] Lu, J.-B., Ma, X.-L., Wang, J.-Q., Liu, J.-C., Xiao, H. and Li, J. (2018). Efficient Nitrogen Fixation via a Redox-Flexible Single-Iron Site with Reverse-Dative Iron to Boron sigma Bonding. J. Phys. Chem. A *122*, 4530–4537.

[102] Wagner, H. E., Frank, N., Barani, E., Anson, C. E., Bayer, L., Powell, A. K., Fink, K. and Breher, F. (2022). Asymmetrically Difunctionalized 1,1-Ferrocenyl Metalloligands and Their Transition Metal Complexes. Eur. J. Inorg. Chem. *2022*, e202100898.

[103] Jiang, Y.-F., Ma, X.-L., Lu, J.-B., Wang, J.-Q., Xiao, H. and Li, J. (2019). N_2 Reduction on Fe-Based Complexes with Different Supporting Main-Group Elements: Critical Roles of Anchor and Peripheral Ligands. Small Methods *3*, 1800340.

[104] Frisch, M. J. *et al.* Gaussian09 Revision E01 (2009). Gaussian Inc. Wallingford CT 2009.

[105] Curtiss, L. A., McGrath, M. P., Blaudeau, J., Davis, N. E., Binning, R. C. and Radom, L. (1995). Extension of Gaussian-2 theory to molecules containing third-row atoms Ga–Kr. J. Chem. Phys. *103*, 6104–6113.

[106] Dolg, M., Wedig, U., Stoll, H. and Preuss, H. (1987). Energy-adjusted ab initio pseudopotentials for the first row transition elements. J. Chem. Phys. *86*, 866–872.

[107] Martin, J. M. L. and Sundermann, A. (2001). Correlation consistent valence basis sets for use with the Stuttgart–Dresden–Bonn relativistic effective core potentials: The atoms Ga–Kr and In–Xe. J. Chem. Phys. *114*, 3408–3420.

[108] Seeger, R. and Pople, J. A. (1977). Self-consistent molecular orbital methods. XVIII. Constraints and stability in Hartree–Fock theory. J. Chem. Phys. *66*, 3045–3050.

[109] Bauernschmitt, R. and Ahlrichs, R. (1996). Stability analysis for solutions of the closed shell Kohn–Sham equation. J. Chem. Phys. *104*, 9047–9052.

[110] Barducci, A., Bussi, G. and Parrinello, M. (2008). Well-Tempered Metadynamics: A Smoothly Converging and Tunable Free-Energy Method. Phys. Rev. Lett. *100*, 020603.

[111] Barducci, A., Bonomi, M. and Parrinello, M. (2011). Metadynamics. WIREs Comput. Mol. Sci. *1*, 826–843.